Computational Mechanics (2020) 65:395–404
https://doi.org/10.1007/s00466-019-01774-4

ORIGINAL PAPER

Anatomically realistic lumen motion representation in patient-specific space–time isogeometric flow analysis of coronary arteries with time-dependent medical-image data

Yuxuan Yu[1] · Yongjie Jessica Zhang[1] · Kenji Takizawa[2] · Tayfun E. Tezduyar[3,4] · Takafumi Sasaki[2]

Received: 1 September 2019 / Accepted: 23 September 2019 / Published online: 10 October 2019

Abstract
Patient-specific computational flow analysis of coronary arteries with time-dependent medical-image data can provide valuable information to doctors making treatment decisions. Reliable computational analysis requires a good core method, high-fidelity space and time discretizations, and an anatomically realistic representation of the lumen motion. The space–time variational multiscale (ST-VMS) method has a good track record as a core method. The ST framework, in a general context, provides higher-order accuracy. The VMS feature of the ST-VMS addresses the computational challenges associated with the multiscale nature of the unsteady flow in the artery. The moving-mesh feature of the ST framework enables high-resolution flow computation near the moving fluid–solid interfaces. The ST isogeometric analysis is a superior discretization method. With IGA basis functions in space, it enables more accurate representation of the lumen geometry and increased accuracy in the flow solution. With IGA basis functions in time, it enables a smoother representation of the lumen motion and a mesh motion consistent with that. With cubic NURBS in time, we obtain a continuous acceleration from the lumen-motion representation. Here we focus on making the lumen-motion representation anatomically realistic. We present a method to obtain from medical-image data in discrete form an anatomically realistic NURBS representation of the lumen motion, without sudden, unrealistic changes introduced by the higher-order representation. In the discrete projection from the medical-image data to the NURBS representation, we supplement the least-squares terms with two penalty terms, corresponding to the first and second time derivatives of the control-point trajectories. The penalty terms help us avoid the sudden unrealistic changes. The computation we present demonstrates the effectiveness of the method.

Keywords Coronary arteries · Patient-specific computational flow analysis · Time-dependent medical-image data · Space–time variational multiscale method · Space–time isogeometric analysis · Anatomically realistic lumen motion · Penalty spline

1 Introduction

Coronary arteries, attached to the heart surface, supply blood to the heart. "Atherosclerotic narrowing" of coronary arteries [1] may lead to the heart attack or "sudden cardiac death" [2]. Such artery diseases are the leading cause of morbidity and mortality among adults today [3]. Patient-specific computational flow analysis of coronary arteries can help doctors explain pathology of atherosclerosis and make treatment decisions. It has been known for quite a while (see,

✉ Yuxuan Yu
yuxuany1@andrew.cmu.edu

Yongjie Jessica Zhang
jessicaz@andrew.cmu.edu

Kenji Takizawa
Kenji.Takizawa@tafsm.org

Tayfun E. Tezduyar
tezduyar@tafsm.org

Takafumi Sasaki
Takafumi.Sasaki@tafsm.org

[1] Department of Mechanical Engineering, Carnegie Mellon University, 5000 Forbes Ave, Pittsburgh, PA 15213, USA

[2] Department of Modern Mechanical Engineering, Waseda University, 3-4-1 Ookubo, Shinjuku-ku, Tokyo 169-8555, Japan

[3] Mechanical Engineering, Rice University, MS 321, 6100 Main Street, Houston, TX 77005, USA

[4] Faculty of Science and Engineering, Waseda University, Tokyo, Japan

for example, [4–6]) that the wall shear stress (WSS) plays a significant role in arterial diseases, and its quantification can help identify the high-probability regions of the disease. Possible connection between the atherosclerosis and the WSS has been reported in several papers [7,8]. Patient-specific computational flow analysis of coronary arteries is appealing in quantifying atherosclerosis diseases based on hemodynamic factors. In this class of computational flow analysis, we use the Space–Time Variational Multiscale (ST-VMS) method [9–11], which serves as the core method, and the ST Isogeometric Analysis (ST-IGA) [9,12,13]. The ST-VMS and ST-IGA give us increased accuracy in the flow solution. The ST-IGA also gives us a smoother and more accurate representation of the lumen geometry and motion. With cubic NURBS in time, we obtain a continuous acceleration from the lumen-motion representation. The higher-order representation in time might introduce sudden, unrealistic lumen motion. Here we focus focus on making the motion representation anatomically realistic.

1.1 Moving-boundary problems

It was shown as early as 2004 [4–6] that there are significant differences in the WSS obtained from blood flow computations with the rigid- and flexible-artery models. This created a strong incentive to conduct blood flow computations with flexible-artery models. Furthermore, it was recognized as early as 2008 [14] that high-refinement mesh layers near the lumen boundary are essential in high-resolution representation of the boundary layers and in accurate calculation of the WSS. In computation of flows with moving boundaries and interfaces (MBI), including fluid–structure interaction (FSI), a moving-mesh method enables mesh-resolution control near the interface and, consequently, high-resolution representation of the boundary layer. Because the coronary arteries undergo large motions during the cardiac cycle, the moving-mesh method will also need to be able to handle large lumen motions. Both the ST [9,15] and Arbitrary Lagrangian–Eulerian (ALE) [16] methods are moving-mesh methods, with the ALE being the earlier and more commonly used one.

The Deforming-Spatial-Domain/Stabilized ST (DSD/SST) method [15,17], the precursor of the ST-VMS, was introduced for FSI and MBI computations. Because the stabilization components of the original DSD/SST are the Streamline-Upwind/Petrov-Galerkin (SUPG) [18] and Pressure-Stabilizing/Petrov-Galerkin [15,19] stabilizations, the method is now also called "ST-SUPS." The VMS components of the ST-VMS are from the residual-based VMS method [20–23]. The ST-VMS has two more stabilization terms beyond those the ST-SUPS has. The ALE-VMS method [23,24] is the VMS version of the ALE. It succeeded the ST-SUPS and ALE-SUPS [25] methods and preceded the ST-VMS.

In the computational flow analysis presented here, the ST framework provides higher-order accuracy in a general context. The VMS feature of the ST-VMS addresses computational challenges associated with multiscale nature of unsteady flow in the arteries. The moving-mesh feature of the ST framework enables high-resolution computation near the lumen boundary as the artery moves.

1.2 ST-IGA

The ST-IGA was introduced in [9]. It is the integration of the ST framework with isogeometric discretization [24,26,27]. First computations with the ST-VMS and ST-IGA were reported in [9] in a 2D context, with IGA basis functions in space for flow past an airfoil, and in both space and time for the advection equation. The stability and accuracy analysis given in [9] for the advection equation showed that using higher-order basis functions in time would be essential in getting full benefit out of using higher-order basis functions in space.

As pointed out in [9,10] and demonstrated in [12,28,29], higher-order NURBS basis functions in time provide a more accurate representation of the motion of the solid surfaces and a mesh motion consistent with that. They also provide more efficiency in temporal representation of the motion and deformation of the volume meshes, and better efficiency in remeshing. The ST framework and NURBS in time also enable, with the "ST-C" method, extracting a continuous representation from the computed data and, in large-scale computations, efficient data compression [11,30–35].

In the computational flow analysis presented here, the ST-IGA gives us increased accuracy in the flow solution and a smoother and more accurate representation of the lumen geometry and motion.

1.3 Motion representation

The ST-IGA with IGA basis functions in time provides a good framework for smooth motion representation. With cubic NURBS in time, the representation gives us continuous acceleration [12], which is key to obtaining a reasonable time-dependent behavior from the calculation of the fluid mechanics forces acting on the moving surface. The desirable features of the ST-IGA have been used in many 3D computations. The classes of problems solved are flapping-wing aerodynamics for an actual locust [12,23,28,36], bioinspired MAVs [29,37–39] and wing-clapping [40,41], separation aerodynamics of spacecraft [42], aerodynamics of horizontal-axis [38,39,43,44] and vertical-axis [45–47] wind-turbines, thermo-fluid analysis of ground vehicles and their tires [11,31], thermo-fluid analysis of disk brakes [32], flow-driven string dynamics in turbomachinery [33–35], and flow analysis of turbocharger turbines [13,48–50].

In the locust flapping-wing aerodynamics [12,23,28,36], for example, the wing-motion data in discrete form, extracted from the high-speed video cameras of the wind tunnel, was least-squares projected to cubic NURBS representation in time. We use the same method here in obtaining the cubic NURBS representation of the lumen motion from the medical-image data in discrete form. With that, we have a continuous acceleration in the lumen-motion representation. However, because of the higher-order nature of the NURBS representation, sometimes we might see sudden unrealistic changes in time. This would degrade the flow solution quality. Here, we propose a remedy for that.

1.4 Penalty least-squares projection

Starting with the method of least-squares projection to cubic NURBS representation given in [12,28], we introduce a penalty least-squares (PLS) projection method to make the lumen-motion representation anatomically realistic in patient-specific computational flow analysis of coronary arteries with time-dependent medical-image data. We supplement the method given in [12,28] with two penalty terms, corresponding to the first and second time derivatives of the control-point trajectories. The penalty terms help us avoid the sudden unrealistic changes and obtain an anatomically realistic NURBS representation of the lumen motion. We, of course, still retain the smooth representation that comes with the NURBS basis functions.

1.5 Outline of the remaining sections

In Sect. 2, we provide the time-dependent anatomical model in terms of the lumen motion, and a mesh motion consistent that. Making the lumen motion anatomically realistic with the PLS projection method is described in Sect. 3. The fluid mechanics computation method and the computational conditions are described in Sect. 4. The results are presented in Sect. 5, and the concluding remarks are given in Sect. 6.

2 Time-dependent anatomical model

We obtain the lumen motion from the coronary artery centerline motion in [1], which is the step-populated and somewhat smoothed version of the centerline motion [51] extracted from MRI data. The cardiac cycle is $T = 1$ s. There are 400 steps in a cardiac cycle, making the time-step size 2.5 ms. The lumen geometry, represented by the lumen boundary mesh, is generated as part of the lumen NURBS mesh. In generating the quadratic NURBS mesh for each time step, we first we create a quadrilateral control mesh for the inlet section and sweep it along the centerline (see [52,53]). Figure 1 shows the lumen geometry at three instants.

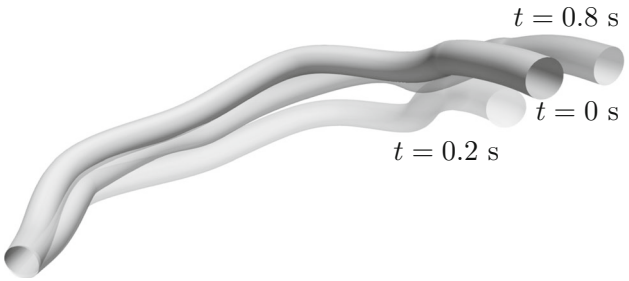

Fig. 1 Lumen geometry at three instants during the cardiac cycle

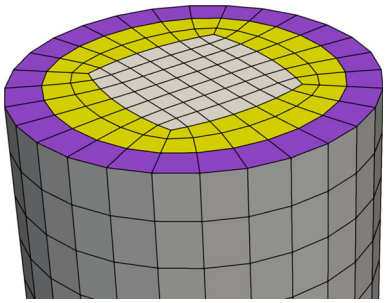

Fig. 2 Control mesh after the Laplacian smoothing. We identify two layered zones: external (purple) and internal (yellow). (Color figure online)

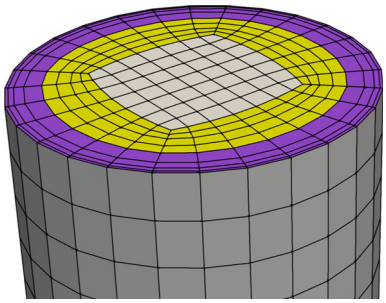

Fig. 3 Control mesh after the refinement for higher-resolution representation of the boundary layers

Next we apply Laplacian smoothing [54] to improve the control mesh quality. Figure 2 shows the control mesh after the Laplacian smoothing. To have higher-resolution representation of the boundary layers, we increase the mesh refinement. We make the number of external-zone layers 4, with a progression factor of 1.8, and the number of internal-zone layers also 4, by evenly splitting the existing layers. The refined mesh has 44,928 control points and 42,315 elements. Figure 3 shows the control mesh after the refinement. Figure 4 shows the control mesh at $t = 0$.

3 Anatomically realistic representation of the lumen motion

Representing the medical-image data given in discrete form with linear basis functions in time does not result in a

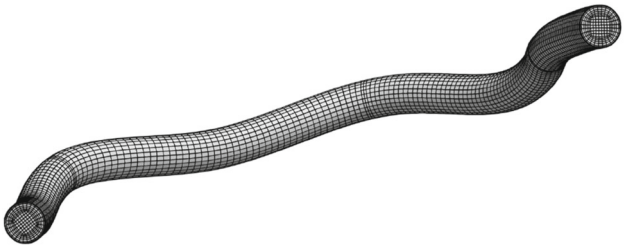

Fig. 4 Control mesh at $t = 0$

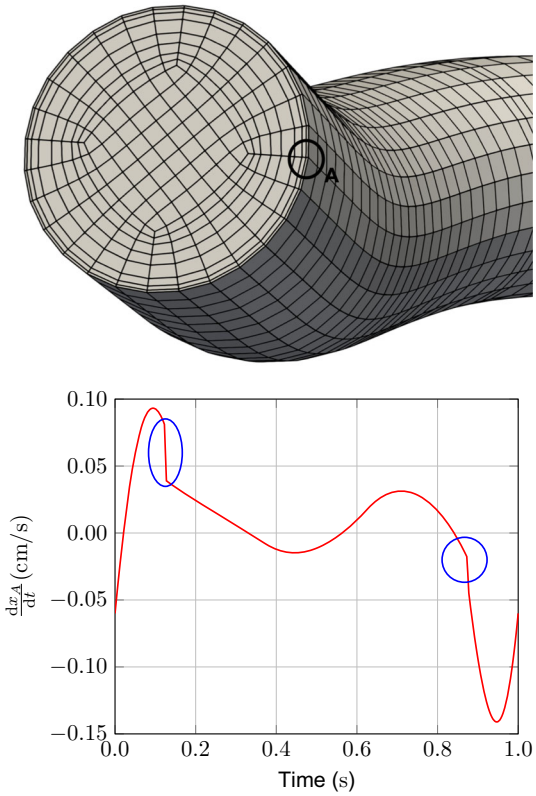

Fig. 5 A control point "A" (top) and the time derivative of the x component of its position (bottom) in linear temporal representation. We see a jump at $t = 0.12$ s, and a kink at $t = 0.87$ s

smooth representation. The first and second derivatives of the control-point trajectories, corresponding to the velocity and acceleration, cannot be expected to be continuous. Figure 5 shows an example. A continuous acceleration is key to obtaining a reasonable time-dependent behavior from the calculation of the fluid mechanics forces acting on the moving arterial wall. We need a smoother representation of the lumen motion.

3.1 NURBS representation of the lumen motion

The ST-IGA with cubic NURBS in time gives us a representation with continuous acceleration [12,28]. In addition, with quadratic NURBS in space, we have increased accuracy in the flow solution and a smoother and more accurate representation of the lumen geometry. Similar to what was done in [12,28] for the locust flapping-wing aerodynamics, the medical-image data in discrete form is least-squares projected to cubic NURBS representation in time. As a consequence of the acceleration being continuous, the WSS will be continuous.

Because of the higher-order nature of the NURBS representation, sometimes we might see sudden unrealistic changes in time. We need to make the representation anatomically realistic.

3.2 Periodic data

The lumen motion is roughly periodic. We generate from that a periodic data set, where the first and last points of the cycle are colocated and have the desired continuity. Thus, a single cycle of lumen motion can be repeated to produce as many cardiac cycles as needed.

To obtain a periodic data set, after the least-squares projection, we extract one cardiac cycle. To maintain continuity, the control points corresponding to the knot at the beginning of the cardiac cycle are colocated with the control points corresponding to the knot at the end of the cardiac cycle (three control points correspond to a given knot). To obtain such repetition, we average those control points. Finally, we insert knots to extract a single cycle. See [28] for more on the process, including figures illustrating the averaging.

3.3 PLS projection

A spatial-control point $\mathbf{x}_A$ will be represented as

$$\mathbf{x}_A = \sum_{\alpha=0}^{n_{\text{ct}}-1} N_{\alpha,3}(\vartheta)\mathbf{x}_A^\alpha, \tag{1}$$

where $\mathbf{x}_A^\alpha$ is the temporal-control point associated with the NURBS basis function $N_{\alpha,3}(\vartheta)$, with ϑ representing the NURBS parametric space. The basis functions are defined over the parametric space given by the open knot vector $\{\vartheta_1, \ \ldots, \ \vartheta_{n_{\text{kt}}}\}$, where n_{ct} and n_{kt} are the number of temporal-control points and knots.

The PLS projection is derived from the functional

$$E_A(\mathbf{x}_A^\alpha) = \sum_{k=0}^{m} \omega_k \left\| \mathbf{x}_A(\tilde{\vartheta}_k) - \tilde{\mathbf{x}}_A(\tilde{\vartheta}_k) \right\|^2 + \lambda_1 \sum_{\alpha=1}^{n_{\text{ct}}-1} \left\| D_t \mathbf{x}_A^\alpha \right\|^2 + \lambda_2 \sum_{\alpha=2}^{n_{\text{ct}}-1} \left\| D_{tt} \mathbf{x}_A^\alpha \right\|^2, \tag{2}$$

where

$$D_t \mathbf{x}_A^\alpha = \mathbf{x}_A^\alpha - \mathbf{x}_A^{\alpha-1}, \tag{3}$$

$$D_{tt} \mathbf{x}_A^\alpha = \mathbf{x}_A^\alpha - 2\mathbf{x}_A^{\alpha-1} + \mathbf{x}_A^{\alpha-2}, \tag{4}$$

m is the number of time steps for the medical-image data, and ω_k, λ_1 and λ_2 are the PLS projection parameters. The parametric value $\tilde{\vartheta}_k$ corresponds to the time step k. It is related to the temporal knot vector $\{\vartheta_1, \ldots, \vartheta_{n_{\text{kt}}}\}$ by the formula $\tilde{\vartheta}_k = \vartheta_1 + k\frac{\vartheta_{n_{\text{kt}}} - \vartheta_1}{m}$ $(k = 0, \ldots, m)$.

The first summation in Eq. (2) represents the discrete least-squares projection, with the option of having different weights for different time steps of the medical-image data. The second and third summations represent the penalty terms corresponding to the first and second time derivatives of the control-point trajectories.

3.4 Selection of the PLS projection parameters

When $\lambda_1 = 0$, $\lambda_2 = 0$, and $\omega_k = 1$, the PLS projection becomes just a least-squares projection, which we will label "LS" for the purpose of presenting the results. When $\omega_k = 1$ and only one of the parameters λ_1 and λ_2 is nonzero, Eq. (2) gives the penalty B-splines [55]. In the computations reported in this article, $\lambda_1 = 1$, $\lambda_2 = 1$, and $[\omega_k] = [1000, 1000, 1, \ldots 1, 1000, 1000]$. The number of elements in time is 240, which represents the three cycles we use to extract the middle cycle and generate periodic data as described in Sect. 3.2.

Figure 6 shows the position and acceleration of a spatial-control point, from the medical-image data and from the LS and PLS projections.

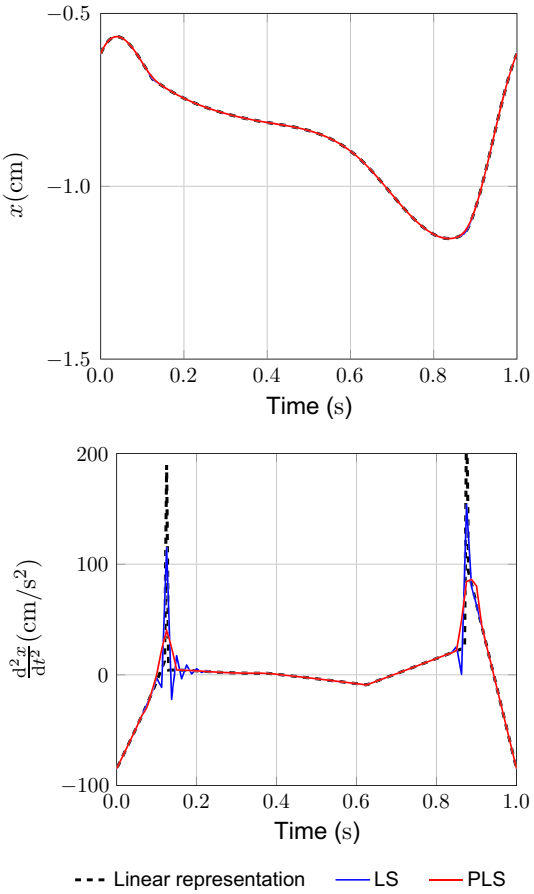

Fig. 6 Position and acceleration of a spatial-control point, from linear representation and cubic NURBS representation with LS and PLS projections

4 Fluid mechanics computation

The arterial diameter D at the inflow is 4.02 mm and the average flow rate Q is 1.08 cm^3/s. The average shear rate in the artery can be estimated from the laminar-flow approximation as $\dot{\gamma} = 32Q/(\pi D^3) = 169$ s^{-1}. As explained in [56,57], the viscosity of the blood can be approximated as a constant when the shear rate is higher than 150 s^{-1}. Therefore we assume the blood to be Newtonian here. The density and kinematic viscosity are 1,060 kg/m^3 and 4.0×10^{-6} m^2/s.

The governing equations are the Navier–Stokes equations of incompressible flow:

$$\rho\left(\frac{\partial \mathbf{u}}{\partial t} + \mathbf{u}\cdot\nabla\mathbf{u} - \mathbf{f}\right) - \nabla\cdot\boldsymbol{\sigma} = \mathbf{0}, \tag{5}$$

$$\nabla\cdot\mathbf{u} = 0, \tag{6}$$

where ρ, $\mathbf{u}$ and $\mathbf{f}$ are the density, velocity and the body force. The stress tensor is defined as $\boldsymbol{\sigma}(\mathbf{u}, p) = -p\mathbf{I} + 2\mu\boldsymbol{\varepsilon}(\mathbf{u})$, where p is the pressure, $\mathbf{I}$ is the identity tensor, $\mu = \rho\nu$ is the viscosity, ν is the kinematic viscosity, and $\boldsymbol{\varepsilon}(\mathbf{u}) = \left(\nabla\mathbf{u} + (\nabla\mathbf{u})^T\right)/2$ is the strain-rate tensor.

4.1 ST-VMS

The ST-SUPS and ST-VMS formulations (see for example [9–11,15,17,58]) are written over a sequence of N ST slabs Q_n, where Q_n is the slice of the ST domain between the time levels t_n and t_{n+1}, and P_n is the lateral boundary of Q_n. At each time step, the integrations are performed over Q_n. The essential and natural boundary conditions are enforced over $(P_n)_{\text{g}}$ and $(P_n)_{\text{h}}$, the complementary subsets of the lateral boundary of the ST slab. The ST basis functions are continuous within a ST slab, but discontinuous from one ST slab to another. The notation $(\cdot)_n^-$ and $(\cdot)_n^+$ will denote the function values at t_n as approached from below and above. Each Q_n is decomposed into elements Q_n^e, where $e = 1, 2, \ldots, (n_{\text{el}})_n$. The subscript n used with n_{el} is for the general case where

the number of ST elements may change from one ST slab to another. The ST-VMS formulation is given as

$$\begin{aligned}
&\int_{Q_n} \mathbf{w}^h \cdot \rho \left(\frac{\partial \mathbf{u}^h}{\partial t} + \mathbf{u}^h \cdot \nabla \mathbf{u}^h - \mathbf{f}^h \right) \mathrm{d}Q \\
&\quad + \int_{Q_n} \boldsymbol{\varepsilon}(\mathbf{w}^h) : \boldsymbol{\sigma}(\mathbf{u}^h, p^h) \mathrm{d}Q - \int_{(P_n)_\mathrm{h}} \mathbf{w}^h \cdot \mathbf{h}^h \mathrm{d}P \\
&\quad + \int_{Q_n} q^h \nabla \cdot \mathbf{u}^h \mathrm{d}Q + \int_{\Omega_n} (\mathbf{w}^h)_n^+ \cdot \rho \left((\mathbf{u}^h)_n^+ - (\mathbf{u}^h)_n^- \right) \mathrm{d}\Omega \\
&\quad + \sum_{e=1}^{(n_\mathrm{el})_n} \int_{Q_n^e} \frac{\tau_\mathrm{SUPS}}{\rho} \left[\rho \left(\frac{\partial \mathbf{w}^h}{\partial t} + \mathbf{u}^h \cdot \nabla \mathbf{w}^h \right) \right. \\
&\qquad \left. + \nabla q^h \right] \cdot \mathbf{r}_\mathrm{M}(\mathbf{u}^h, p^h) \mathrm{d}Q \\
&\quad + \sum_{e=1}^{(n_\mathrm{el})_n} \int_{Q_n^e} \nu_\mathrm{LSIC} \nabla \cdot \mathbf{w}^h \rho r_\mathrm{C}(\mathbf{u}^h) \mathrm{d}Q \\
&\quad - \sum_{e=1}^{(n_\mathrm{el})_n} \int_{Q_n^e} \tau_\mathrm{SUPS} \mathbf{w}^h \cdot \left(\mathbf{r}_\mathrm{M}(\mathbf{u}^h, p^h) \cdot \nabla \mathbf{u}^h \right) \mathrm{d}Q \\
&\quad - \sum_{e=1}^{(n_\mathrm{el})_n} \int_{Q_n^e} \frac{\tau_\mathrm{SUPS}^2}{\rho} \mathbf{r}_\mathrm{M}(\mathbf{u}^h, p^h) \cdot \left(\nabla \mathbf{w}^h \right) \cdot \mathbf{r}_\mathrm{M}(\mathbf{u}^h, p^h) \mathrm{d}Q \\
&= 0. \qquad (7)
\end{aligned}$$

Here

$$\mathbf{r}_\mathrm{M}(\mathbf{u}^h, p^h) = \rho \left(\frac{\partial \mathbf{u}^h}{\partial t} + \mathbf{u}^h \cdot \nabla \mathbf{u}^h - \mathbf{f}^h \right) - \nabla \cdot \boldsymbol{\sigma}(\mathbf{u}^h, p^h), \qquad (8)$$

$$r_\mathrm{C}(\mathbf{u}^h) = \nabla \cdot \mathbf{u}^h \qquad (9)$$

are the residuals of the momentum equation and incompressibility constraint, and τ_SUPS and ν_LSIC are the stabilization parameters. There are many ways of defining these stabilization parameters (for examples, see [11,17,43,58–61]). Here the stabilization parameters are those given by Eqs. (2.4)–(2.9) in [45]. We calculate the WSS by using the expression given by Eq. (5.119) in [23].

4.2 Boundary and starting conditions

At the inflow boundary, we specify the velocity profile as a function of time. The velocity profile is generated by applying the Womersley solution [62,63] with 400 Fourier coefficients. The corresponding time-dependent volumetric flow rate is shown in Fig. 7. The Reynolds number based on this flow rate varies from 45 to 300. The inflow data is least-squares projected to cubic NURBS representation in time. At the outflow the boundary condition is stress-free. The inflow and outflow boundaries are indicated in Fig. 8. We perform the flow computation with two different representations of the lumen motion: linear representation in time and cubic NURBS representation in time with PLS projection. We start the lumen motion suddenly at some instant in the cardiac cycle and expect that the solution will settle within one or two cardiac cycles. We compute for three cardiac cycles.

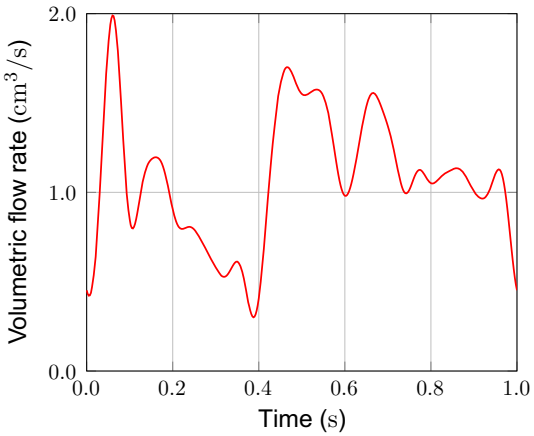

Fig. 7 Volumetric flow rate

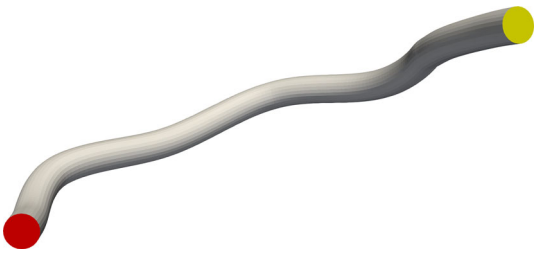

Fig. 8 Inflow (red) and outflow (yellow) boundaries. (Color figure online)

5 Results

First we compare cubic-NURBS lumen-motion representation with LS and PLS projections. After that we compare the flow computations based on lumen-motion with linear and PLS-projected cubic NURBS representations.

5.1 Cubic-NURBS lumen-motion representation with LS and PLS projections

Figure 9 shows the lumen volume and its first and second time derivatives, based on linear representation and cubic NURBS representation with LS and PLS projections. Cubic NURBS representation, as expected, with both LS and PLS projections, brings a smoothness that we cannot get from linear representation. For the first derivative, with the PLS projection we circumvent the sudden, unrealistic changes introduced by the higher-order representation at around 0.12 s. We make a similar observation for the second derivative, this time at instants: 0.12 s and 0.87 s.

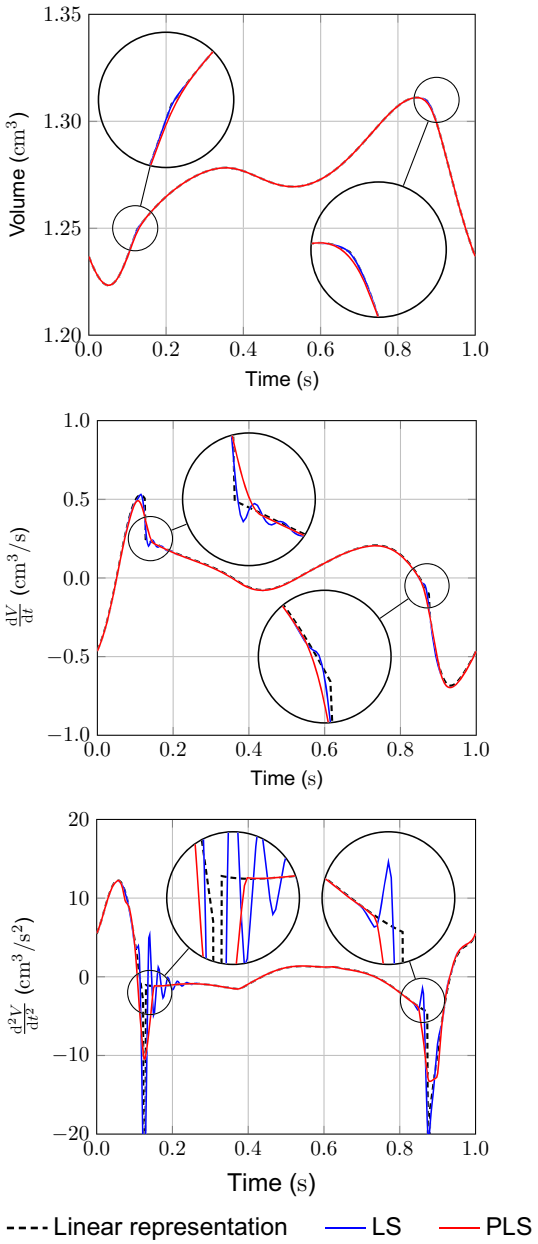

Fig. 9 Lumen volume and its first and second time derivatives, based on linear representation and cubic NURBS representation with LS and PLS projections

Figure 10 shows, among all the spatial-control points on the lumen boundary, the maximum difference between the linear and PLS-projected cubic NURBS representations. This deviation from the medical-image data is actually a small price for an anatomically realistic smooth representation of the lumen motion. The maximum difference is about 0.2 mm, occurring at around 0.12 s. Compared to the centerline length, which is over 100 mm (see Fig. 11 for the model length scales), the difference is about 0.2 %. It is also within the spatial resolution (0.45 mm) of the images [51].

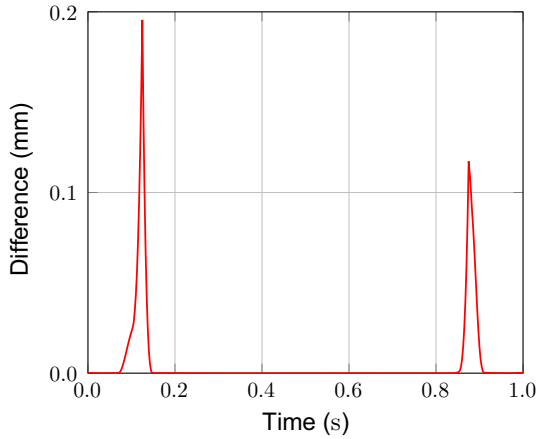

Fig. 10 Among all the spatial-control points on the lumen boundary, the maximum difference between the linear and PLS-projected cubic NURBS representations

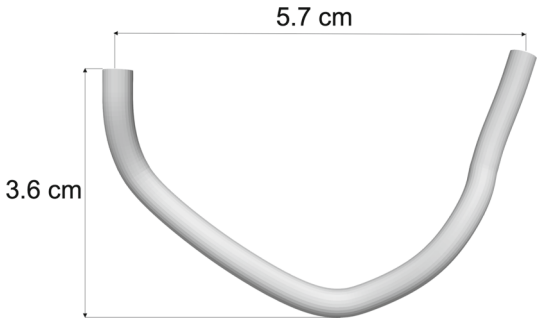

Fig. 11 Model length scales

5.2 Flow computations based on lumen-motion with linear and PLS-projected cubic NURBS representations

In both computations, the mesh motion is consistent with the lumen-motion representation. We use 5 ST slabs for each of the 80 elements of the cubic NURBS representation in time, and that makes the time-step size 2.5×10^{-3} s. The number of nonlinear iterations per time step is 3, and number GMRES iterations per nonlinear iteration is 400.

Figure 12 shows the mass balance for the PLS-projected cubic NURBS representation. By checking the mass balance, we are following an old custom that goes back to early arterial FSI computations with the ST-SUPS (see, for example, [63–66]). The objective is to make sure that the number of GMRES iterations is high enough for the part of the equation system associated with the incompressibility constraint, with the convergence measured not only by the residual decay, but also by the mass balance. Here the derivative of the lumen volume is calculated from the boundary integral of the normal component of the mesh velocity.

Smooth and anatomically realistic representation of the lumen motion makes the WSS calculation more reliable. Fig-

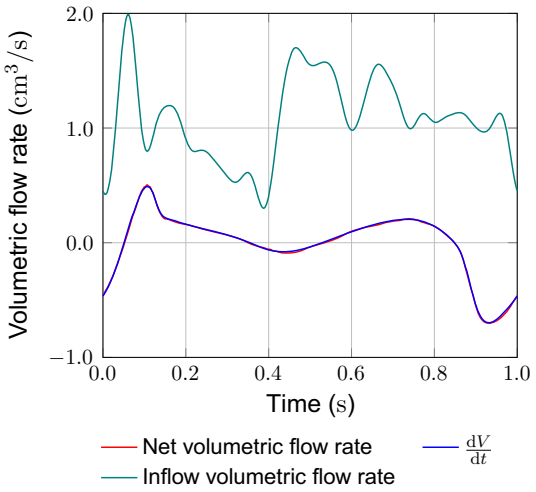

Fig. 12 Mass balance for the PLS-projected cubic NURBS representation

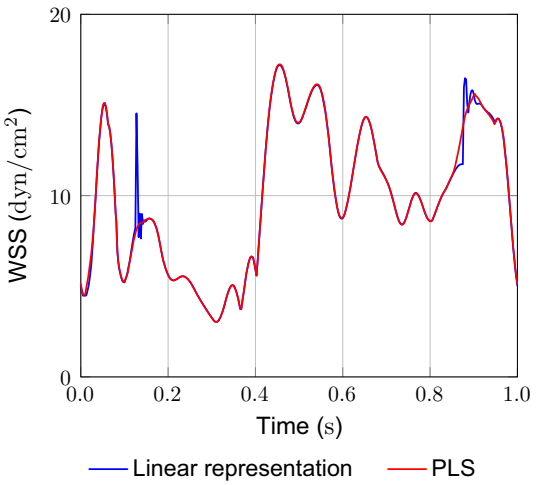

Fig. 13 Spatially-maximum WSS from flow computations based on lumen-motion with linear and PLS-projected cubic NURBS representations

ure 13 shows the spatially-maximum WSS. As can be seen from the figure, with the PLS-projected cubic NURBS representation, we circumvent the sudden, unrealistic changes at around 0.12 s and 0.87 s. Figure 14 shows the spatial distribution of the WSS at $t = 0.1275$ s. In the linear-representation case, the high-WSS distribution we see at the lower part of the artery is consistent with the spikes we see at around 0.12 s in Fig. 13.

6 Concluding remarks

In making treatment decisions related to coronary arteries, patient-specific computational flow analysis with time-dependent medical-image data can play a significant role. A good core computational method, high-fidelity space and

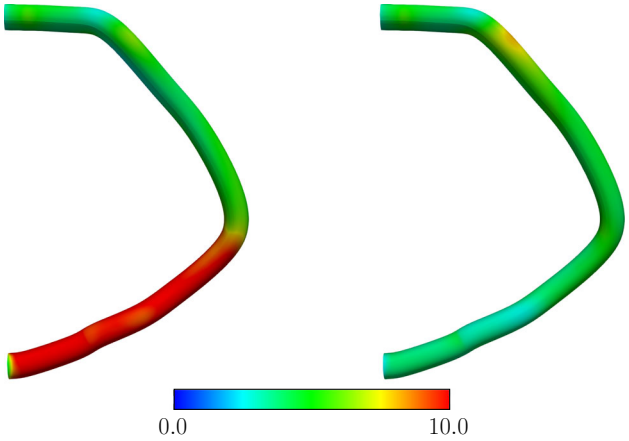

Fig. 14 Spatial distribution of the WSS (dyn/cm^2) at $t = 0.1275$ s, from flow computations based on lumen motion with linear (left) and PLS-projected cubic NURBS (right) representations. The top end of the artery is the inflow end

time discretizations, and an anatomically realistic representation of the lumen motion would make the computational analysis more reliable. To that end, we have proposed in this article a method for anatomically realistic representation of the lumen motion. The method is used in combination with the ST-VMS, which has a good track record as a core method, and the ST-IGA, which is a superior discretization method. The ST framework, in a general context, provides higher-order accuracy. The VMS feature of the ST-VMS addresses the computational challenges associated with the multiscale nature of the unsteady flow in the artery. The moving-mesh feature of the ST framework enables high-resolution flow computation near the moving fluid–solid interfaces. The ST-IGA, with IGA basis functions in space, enables more accurate representation of the lumen geometry and increased accuracy in the flow solution. With IGA basis functions in time, it enables a smoother representation of the lumen motion and a mesh motion consistent with that. With cubic NURBS in time, we obtain a continuous acceleration from the lumen-motion representation, which is key to obtaining a reasonable time-dependent behavior from the calculation of the fluid mechanics forces acting on the moving surface. The method we propose here for obtaining from medical-image data in discrete form an anatomically realistic NURBS representation of the lumen motion circumvents the sudden, unrealistic changes that might be introduced by the higher-order representation. In the discrete projection from the medical-image data to the NURBS representation, we supplement the least-squares terms with two penalty terms, corresponding to the first and second time derivatives of the control-point trajectories. The PLS projection helps us avoid the sudden unrealistic changes. The test computations presented demonstrate that. In the test computations, cubic NURBS representation, as expected, brings a smoothness that we cannot get from linear representation. Beyond

that, the PLS-projected cubic NURBS representation circumvents the sudden, unrealistic changes introduced by the higher-order representation. It is known that the WSS plays a significant role in arterial diseases, and its quantification can help identify the high-probability regions of the disease. Smooth and anatomically realistic representation of the coronary artery lumen motion makes the WSS calculation more reliable, and this has also been demonstrated with the test computations presented.

Acknowledgements Y. Yu and Y.J. Zhang were supported in part by NSF CAREER Award OCI-1149591. This work was also supported (K. Takizawa and T. Sasaki) in part by JST-CREST; Grant-in-Aid for Scientific Research (A) 18H04100 from Japan Society for the Promotion of Science; and Rice–Waseda research agreement. It was also supported (T.E. Tezduyar) in part by Top Global University Project of Waseda University.

References

1. Takizawa K, Torii R, Takagi H, Tezduyar TE, Xu XY (2014) Coronary arterial dynamics computation with medical-image-based time-dependent anatomical models and element-based zero-stress state estimates. Comput Mech 54:1047–1053
2. Arbab-Zadeh A, Nakano M, Virmani R, Fuster V (2012) Acute coronary events. Circulation 125(9):1147–1156
3. McGovern PG, Pankow JS, Shahar E, Doliszny KM, Folsom AR, Blackburn H, Luepker RV (1996) Recent trends in acute coronary heart diseasemortality, morbidity, medical care, and risk factors. N Engl J Med 334(14):884–890
4. Torii R, Oshima M, Kobayashi T, Takagi K, Tezduyar TE (2004) Computation of cardiovascular fluid–structure interactions with the DSD/SST method. In: Proceedings of the 6th world congress on computational mechanics (CD-ROM). Beijing, China
5. Torii R, Oshima M, Kobayashi T, Takagi K, Tezduyar TE (2004) Influence of wall elasticity on image-based blood flow simulations. Trans Jpn Soc Mech Eng Ser A 70:1224–1231 in Japanese
6. Torii R, Oshima M, Kobayashi T, Takagi K, Tezduyar TE (2006) Computer modeling of cardiovascular fluid-structure interactions with the deforming-spatial-domain/stabilized space–time formulation. Comput Methods Appl Mech Eng 195:1885–1895
7. Gijsen FJH, Wentzel JJ, Thury A, Mastik F, Schaar JA, Schuurbiers JC, Slager CJ, van der Giessen WJ, de Feyter PJ, van der Steen AF, Serruys PW (2008) Strain distribution over plaques in human coronary arteries relates to shear stress. Am J Physiol Heart Circ Physiol 295(4):H1608–H1614
8. Slager CJ, Wentzel JJ, Gijsen FJH, Thury A, der Wal ACV, Schaar JA, Serruys PW (2005) The role of shear stress in the destabilization of vulnerable plaques and related therapeutic implications. Nat Clin Practice Cardiovasc Med 2(9):456–464
9. Takizawa K, Tezduyar TE (2011) Multiscale space-time fluid-structure interaction techniques. Comput Mech 48:247–267
10. Takizawa K, Tezduyar TE (2012) Space–time fluid-structure interaction methods. Math Models Methods Appl Sci 22(supp02):1230001
11. Takizawa K, Tezduyar TE, Kuraishi T (2015) Multiscale ST methods for thermo-fluid analysis of a ground vehicle and its tires. Math Models Methods Appl Sci 25:2227–2255
12. Takizawa K, Henicke B, Puntel A, Spielman T, Tezduyar TE (2012) Space-time computational techniques for the aerodynamics of flapping wings. J Appl Mech 79:010903
13. Takizawa K, Tezduyar TE, Otoguro Y, Terahara T, Kuraishi T, Hattori H (2017) Turbocharger flow computations with the space–time isogeometric analysis (ST-IGA). Comput Fluids 142:15–20
14. Tezduyar TE, Schwaab M, Sathe S (2009) Sequentially-coupled arterial fluid-structure interaction (SCAFSI) technique. Comput Methods Appl Mech Eng 198:3524–3533
15. Tezduyar TE (1992) Stabilized finite element formulations for incompressible flow computations. Adv Appl Mech 28:1–44
16. Hughes TJR, Liu WK, Zimmermann TK (1981) Lagrangian–Eulerian finite element formulation for incompressible viscous flows. Comput Methods Appl Mech Eng 29:329–349
17. Tezduyar TE, Sathe S (2007) Modeling of fluid-structure interactions with the space–time finite elements: solution techniques. Int J Numer Meth Fluids 54:855–900
18. Brooks AN, Hughes TJR (1982) Streamline upwind/Petrov–Galerkin formulations for convection dominated flows with particular emphasis on the incompressible Navier–Stokes equations. Comput Methods Appl Mech Eng 32:199–259
19. Tezduyar TE, Mittal S, Ray SE, Shih R (1992) Incompressible flow computations with stabilized bilinear and linear equal-order-interpolation velocity-pressure elements. Comput Methods Appl Mech Eng 95:221–242
20. Hughes TJR (1995) Multiscale phenomena: Green's functions, the Dirichlet-to-Neumann formulation, subgrid scale models, bubbles, and the origins of stabilized methods. Comput Methods Appl Mech Eng 127:387–401
21. Hughes TJR, Oberai AA, Mazzei L (2001) Large eddy simulation of turbulent channel flows by the variational multiscale method. Phys Fluids 13:1784–1799
22. Bazilevs Y, Calo VM, Cottrell JA, Hughes TJR, Reali A, Scovazzi G (2007) Variational multiscale residual-based turbulence modeling for large eddy simulation of incompressible flows. Comput Methods Appl Mech Eng 197:173–201
23. Bazilevs Y, Takizawa K, Tezduyar TE (2013) Computational fluid-structure interaction: methods and applications. Wiley, Hoboken. ISBN 978-0470978771
24. Bazilevs Y, Calo VM, Hughes TJR, Zhang Y (2008) Isogeometric fluid-structure interaction: theory, algorithms, and computations. Comput Mech 43:3–37
25. Kalro V, Tezduyar TE (2000) A parallel 3D computational method for fluid-structure interactions in parachute systems. Comput Methods Appl Mech Eng 190:321–332
26. Hughes TJR, Cottrell JA, Bazilevs Y (2005) Isogeometric analysis: CAD, finite elements, NURBS, exact geometry, and mesh refinement. Comput Methods Appl Mech Eng 194:4135–4195
27. Bazilevs Y, Calo VM, Zhang Y, Hughes TJR (2006) Isogeometric fluid-structure interaction analysis with applications to arterial blood flow. Comput Mech 38:310–322
28. Takizawa K, Henicke B, Puntel A, Kostov N, Tezduyar TE (2012) Space-time techniques for computational aerodynamics modeling of flapping wings of an actual locust. Comput Mech 50:743–760
29. Takizawa K, Kostov N, Puntel A, Henicke B, Tezduyar TE (2012) Space-time computational analysis of bio-inspired flapping-wing aerodynamics of a micro aerial vehicle. Comput Mech 50:761–778
30. Takizawa K, Tezduyar TE (2014) Space-time computation techniques with continuous representation in time (ST-C). Comput Mech 53:91–99
31. Takizawa K, Tezduyar TE (2016) New directions in space-time computational methods. In: Bazilevs Y, Takizawa K (eds) Advances in computational fluid-structure interaction and flow simulation: new methods and challenging computations. Modeling and simulation in science, engineering and technology. Springer, Berlin, pp 159–178. ISBN 978-3-319-40825-5
32. Takizawa K, Tezduyar TE, Kuraishi T, Tabata S, Takagi H (2016) Computational thermo-fluid analysis of a disk brake. Comput Mech 57:965–977

33. Takizawa K, Tezduyar TE, Hattori H (2017) Computational analysis of flow-driven string dynamics in turbomachinery. Comput Fluids 142:109–117
34. Komiya K, Kanai T, Otoguro Y, Kaneko M, Hirota K, Zhang Y, Takizawa K, Tezduyar TE, Nohmi M, Tsuneda T, Kawai M, Isono M (2019) Computational analysis of flow-driven string dynamics in a pump and residence time calculation. In: IOP conference series earth and environmental science, vol 240, p 062014
35. Kanai T, Takizawa K, Tezduyar TE, Komiya K, Kaneko M, Hirota K, Nohmi M, Tsuneda T, Kawai M, Isono M (2019) Methods for computation of flow-driven string dynamics in a pump and residence time. Math Models Methods Appl Sci 29:839–870
36. Takizawa K, Henicke B, Puntel A, Kostov N, Tezduyar TE (2013) Computer modeling techniques for flapping-wing aerodynamics of a locust. Comput Fluids 85:125–134
37. Takizawa K, Tezduyar TE, Kostov N (2014) Sequentially-coupled space-time FSI analysis of bio-inspired flapping-wing aerodynamics of an MAV. Comput Mech 54:213–233
38. Takizawa K, Bazilevs Y, Tezduyar TE, Hsu M-C, Øiseth O, Mathisen KM, Kostov N, McIntyre S (2014) Engineering analysis and design with ALE-VMS and space-time methods. Arch Comput Methods Eng 21:481–508
39. Takizawa K (2014) Computational engineering analysis with the new-generation space-time methods. Comput Mech 54:193–211
40. Takizawa K, Tezduyar TE, Buscher A, Asada S (2014) Space-time interface-tracking with topology change (ST-TC). Comput Mech 54:955–971
41. Takizawa K, Tezduyar TE, Buscher A (2015) Space-time computational analysis of MAV flapping-wing aerodynamics with wing clapping. Comput Mech 55:1131–1141
42. Takizawa K, Montes D, Fritze M, McIntyre S, Boben J, Tezduyar TE (2013) Methods for FSI modeling of spacecraft parachute dynamics and cover separation. Math Models Methods Appl Sci 23:307–338
43. Takizawa K, Tezduyar TE, McIntyre S, Kostov N, Kolesar R, Habluetzel C (2014) Space-time VMS computation of wind-turbine rotor and tower aerodynamics. Comput Mech 53:1–15
44. Bazilevs Y, Takizawa K, Tezduyar TE, Hsu M-C, Kostov N, McIntyre S (2014) Aerodynamic and FSI analysis of wind turbines with the ALE-VMS and ST-VMS methods. Arch Comput Methods Eng 21:359–398
45. Takizawa K, Tezduyar TE, Mochizuki H, Hattori H, Mei S, Pan L, Montel K (2015) Space-time VMS method for flow computations with slip interfaces (ST-SI). Math Models Methods Appl Sci 25:2377–2406
46. Korobenko A, Bazilevs Y, Takizawa K, Tezduyar TE (2018) Recent advances in ALE-VMS and ST-VMS computational aerodynamic and FSI analysis of wind turbines. In: Tezduyar TE (ed) Frontiers in computational fluid–structure interaction and flow simulation: research from lead investigators under forty—2018. Modeling and simulation in science, engineering and technology. Springer, Berlin, pp 253–336. ISBN 978-3-319-96468-3
47. Korobenko A, Bazilevs Y, Takizawa K, Tezduyar TE (2018) Computer modeling of wind turbines: 1. ALE-VMS and ST-VMS aerodynamic and FSI analysis. Arch Comput Methods Eng 26:1059–1099
48. Otoguro Y, Takizawa K, Tezduyar TE (2017) Space-time VMS computational flow analysis with isogeometric discretization and a general-purpose NURBS mesh generation method. Comput Fluids 158:189–200
49. Otoguro Y, Takizawa K, Tezduyar TE (2018) A general-purpose NURBS mesh generation method for complex geometries. In: Tezduyar TE (ed) Frontiers in computational fluid–structure interaction and flow simulation: research from lead investigators under forty—2018. Modeling and simulation in science, engineering and technology. Springer, Berlin, pp 399–434. ISBN 978-3-319-96468-3
50. Otoguro Y, Takizawa K, Tezduyar TE, Nagaoka K, Mei S (2019) Turbocharger turbine and exhaust manifold flow computation with the space–time variational multiscale method and isogeometric analysis. Comput Fluids 179:764–776
51. Torii R, Keegan J, Wood NB, Dowsey AW, Hughes AD, Yang G-Z, Firmin DN, Thom SAM, Xu XY (2010) MR image-based geometric and hemodynamic investigation of the right coronary artery with dynamic vessel motion. Ann Biomed Eng 38:2606–2620
52. Zhang Y, Bazilevs Y, Goswami S, Bajaj C, Hughes TJR (2007) Patient-specific vascular NURBS modeling for isogeometric analysis of blood flow. Comput Methods Appl Mech Eng 196:2943–2959
53. Urick B, Sanders TM, Hossain SS, Zhang YJ, Hughes TJR (2019) Review of patient-specific vascular modeling: template-based isogeometric framework and the case for CAD. Arch Comput Methods Eng 26(2):381–404
54. Zhang YJ, Bajaj C, Xu G (2009) Surface smoothing and quality improvement of quadrilateral/hexahedral meshes with geometric flow. Commun Numer Methods Eng 25(1):1–18
55. Eilers PHC, Marx BD (1996) Flexible smoothing with B-splines and penalties. Stat Sci 11(2):89–102
56. Wells RE Jr, Merrill EW (1961) Shear rate dependence of the viscosity of whole blood and plasma. Science 133(3455):763–764
57. Torii R, Oshima M, Kobayashi T, Takagi K, Tezduyar TE (2007) Numerical investigation of the effect of hypertensive blood pressure on cerebral aneurysm—dependence of the effect on the aneurysm shape. Int J Numer Meth Fluids 54:995–1009
58. Tezduyar TE (2003) Computation of moving boundaries and interfaces and stabilization parameters. Int J Numer Meth Fluids 43:555–575
59. Hsu M-C, Bazilevs Y, Calo VM, Tezduyar TE, Hughes TJR (2010) Improving stability of stabilized and multiscale formulations in flow simulations at small time steps. Comput Methods Appl Mech Eng 199:828–840
60. Takizawa K, Tezduyar TE, Otoguro Y (2018) Stabilization and discontinuity-capturing parameters for space-time flow computations with finite element and isogeometric discretizations. Comput Mech 62:1169–1186
61. Kuraishi T, Takizawa K, Tezduyar TE (2019) Tire aerodynamics with actual tire geometry, road contact and tire deformation. Comput Mech 63:1165–1185
62. Womersley JR (1955) Method for the calculation of velocity, rate of flow and viscous drag in arteries when the pressure gradient is known. J Physiol 127:553–563
63. Takizawa K, Christopher J, Tezduyar TE, Sathe S (2010) Space-time finite element computation of arterial fluid-structure interactions with patient-specific data. Int J Numer Methods Biomed Eng 26:101–116
64. Tezduyar TE, Sathe S, Cragin T, Nanna B, Conklin BS, Pausewang J, Schwaab M (2007) Modeling of fluid-structure interactions with the space-time finite elements: arterial fluid mechanics. Int J Numer Meth Fluids 54:901–922
65. Tezduyar TE, Takizawa K, Moorman C, Wright S, Christopher J (2010) Multiscale sequentially-coupled arterial FSI technique. Comput Mech 46:17–29
66. Takizawa K, Moorman C, Wright S, Christopher J, Tezduyar TE (2010) Wall shear stress calculations in space-time finite element computation of arterial fluid-structure interactions. Comput Mech 46:31–41